Electrochimica Acta 145 (2014) 259–269

Contents lists available at ScienceDirect

Electrochimica Acta

journal homepage: www.elsevier.com/locate/electacta

Nitrogen and Sulfur Co-doped Mesoporous Carbon Materials as Highly Efficient Electrocatalysts for Oxygen Reduction Reaction

Jingjing Shi [a], Xuejun Zhou [a], Pan Xu [a], Jinli Qiao [a,*], Zhongwei Chen [b,*], Yuyu Liu [c,*]

[a] College of Environmental Science and Engineering, Donghua University, 2999 Ren'min North Road, Shanghai 201620, PR China
[b] Department of Chemical Engineering, E6-2006, University of Waterloo, 200 University Avenue West, Waterloo, ON, N2L 3G1, Canada
[c] Multidisciplinary Research on the Circulation of Waste Resources,Graduate School of Environmental Studies, Tohoku University, Aramaki,aza Aoba 6-6-11, Aoba-ku, Sendai 980-8579, Japan

ARTICLE INFO

Article history:
Received 30 May 2014
Received in revised form 29 July 2014
Accepted 18 August 2014
Available online 2 September 2014

Keywords:
Mesoporous carbon material
N and S co-doping
Oxygen reduction reaction
Proton-exchange membrane fuel cell

ABSTRACT

Nitrogen and sulfur co-doped mesoporous carbon materials are synthesized by pyrolyzing $FeSO_4$ + poly (ethyleneimine) + template SiO_2 mixture at a high temperature without additional dopant precursors. For post-treatment, acid leaching is used to remove the metal, and the heat-treatment is tailored to optimize the catalytic activity of the catalysts toward the oxygen reduction reaction (ORR) in acidic solution. Scanning electron microscopy, X-ray diffraction, low-temperature N_2 adsorption, X-ray photoelectron spectroscopy and inductively coupled plasma are used to characterize the catalysts' morphologies, structures, and compositions. Rotating disk electrode and rotating ring-disk electrode techniques are employed to quantitatively obtain the ORR kinetic constants and determine the reaction mechanisms. The ORR activity is highly improved by reheating the catalyst after H_2SO_4 leaching with improved half-wave potential of 0.68 V vs. RHE, and ORR electron number larger than 3.76. Moreover, increasing the catalyst loading of 800 $\mu g\,cm^{-2}$ exhibits only ~36 mV deviation from Pt/C. It is believed that the synergetic effect between the Fe-, N- and S-containing active sites and the modified carbon matrix structure due to H_2SO_4 leaching and reheating should make contribution to the high ORR activity.

1. Introduction

In the face of rising energy demands and the concurrent need for environmental protection, polymer electrolyte membrane (PEM) fuel cells are considered to be promising energy conversion devices due to their high energy efficiency and low/zero emissions. However, the most practical PEM fuel cell cathode catalysts remain expensive Pt-based materials, hindering this technology's commercialization; in addition to their high cost due to the scarcity of Pt, these catalysts are not sufficiently stable and exhibit unsatisfactory catalytic activity towards the oxygen reduction reaction (ORR). To overcome these challenges, two strategies are normally proposed: (1) lowering the Pt loading and (2) completely replacing Pt with non-precious metal (NPM) catalysts. Cheap, abundant NPM catalysts are believed to be the best long-term, sustainable solutions for large-scale applications of PEM fuel cell technology.

Regarding NPM catalysts, extensive work have been done to develop transition metal N-containing complexes, conductive polymer-based catalysts, transition metal chalcogenides, metal oxides/carbides/nitrides/oxynitrides/carbonitrides, and enzymatic compounds [1]. Among these candidates, transition metal N-containing complexes supported on carbon materials (M-N_X/C) have received intensive attention over the past few decades because of their relatively high ORR activity, especially for Fe- and Co-centered catalysts [2,3]. However, compared with Pt-based catalysts, these alternatives usually suffer from high activation polarization and poor durability, partly caused by the instability of transition metals. For this reason, developing "metal-free" catalysts has been actively pursued, as this would not only provide more stable catalysts but also yield some defined structures for fundamental understanding.

Normally, "metal-free" catalysts exhibit better stability than transition metal N-containing complexes because there are no issues related to metal dissolution and poisoning as observed from those metal-containing catalysts. One typical candidate from the work of Gong et al. [4], a "metal-free" catalyst with N-containing polymer (poly(diallyldimethylammonium chloride) modified carbon nanotube arrays, catalyzed a more efficient 4e$^-$ORR process in alkaline medium. Nitrogen-doped carbon nanotubes [5–7],

* Corresponding authors. Tel: +86 21 67792379. Fax: +86 21 67792159.
E-mail addresses: qiaojl@dhu.edu.cn (J. Qiao), zhwchen@uwaterloo.ca (Z. Chen), liu@mail.kankyo.tohoku.ac.jp (Y. Liu).

http://dx.doi.org/10.1016/j.electacta.2014.08.091
0013-4686/

graphene [8,9] and carbon black [10] have also been reported as efficient ORR catalysts in alkaline electrolytes. As yet, their insufficient catalytic ORR activity still remains a great challenge when compared with Pt-based catalysts. More importantly, the resulting catalysts yield poor ORR activity particularly in acidic solutions [4,11]. Since that the proton exchange membrane fuel cells are in much wider use than alkaline fuel cells for their high energy density and power density, more work is definitely necessary to improve the catalytic activity and stability of the NPM catalysts [2,12–14] in acidic solution.

In the enhancement of catalytic activity and stability, a NPM catalyst's specific surface area and porous structure, which determine the accessibility of active sites and the transport properties of the ORR-relevant species (H^+, e^-, O_2, H_2O, and OH^-), play important roles in its performance. With respect to this, the template method has recently drawn significant attention for obtaining the specified morphologies and predetermined mesoporous structures [15–20]. Several kinds of templates have been employed for different microstructures—for instance, silica colloid for interconnected vesicle-like frameworks [15–18], SBA-15 for a well-defined linear array [19], and montmorillonite for nanosheet-like structures [20]. Unfortunately, owing to their low ORR catalytic activity, mesoporous carbon materials derived via a template method are commonly used as catalyst supports rather than catalysts. To make these mesoporous materials exhibit catalytic ORR activity, functionalizing the materials using heteroatoms seemes to be an effective approach [20,21].

More recently, certain types of heteroatom-doped nanocarbon materials, in particular nitrogen- and sulfur-doped, have shown high activity for the ORR. In fact, N has an extra electron that can improve the electron donation and in turn enhance catalyst performance. On the other hand, the electronegativity of S is close to that of carbon. Synergy between these two elements is believed to create new non-electroneutral sites, such as favorable positively charged sites for side-on O_2 surface adsorption, promoting catalytic ORR activity [22]. Up to now, extensive research efforts have been made to explore N-doped non-noble metal [2,23–25] or "metal-free" [5,10] ORR catalysts. S-doped ones, on the other hand, in particular S-doped carbon materials as well as N and S co-doped carbon materials have not been studied extensively [26–29].

In this paper, mesoporous carbon materials co-doped using N and S, with high surface area, high porosity, and a large active site density, were designed and synthesized by mixing ferrous sulfate ($FeSO_4$ $7H_2O$) and poly(ethyleneimine) (PEI) in one-step procedure without adding any additional N or S precursors. In the synthesis process, PEI was used as the N and C source, and nanoscale SiO_2 was used as the sacrificial template for pore structure generation. $FeSO_4$ $7H_2O$ was used as the precursor of metal and S source without needing to add extra S precursor. In particular, transition metal Fe was also used to tune the pore structures synergistically with SiO_2 which was removed by acid-leaching after heat-treatment to obtain final catalysts and, thus to improve the durability of catalysts at the same time. The effects of post-treatment methods on catalytic ORR activity were thoroughly examined by scanning electron microscopy (SEM), X-ray diffraction (XRD), low-temperature N_2 adsorption, X-ray photoelectron spectroscopy (XPS) and inductively coupled plasma (ICP). The catalytic ORR activities of the resultant highly porous catalysts were studied by linear sweep voltammetry (LSV) employing rotating disk electrode (RDE) and rotating ring-disk electrode (RRDE) techniques to quantitatively obtain the ORR kinetic constants and the catalysts' possible reaction mechanisms.

2. Experimental

2.1. Preparation of catalysts

The catalysts were prepared by homogeneously dispersing iron and PEI precursors onto the surface of SiO_2 (Hangzhou Wanjing New Material Co., Ltd 10–15 nm in diameter). In a typical synthesis process, 4.5 g PEI solution (50 wt. %, Sigma–Aldrich, molecular weight 2000) was added into a calculated amount of SiO_2 solution (the PEI content with respect to the silica was 45 wt.%, silica amount: 5 g) under magnetic stirring to form a PEI-SiO_2 mixed solution. Then, a solution of $FeSO_4$ $7H_2O$ (Sinopharm Chemical Reagent Co., Ltd Fe:PEI = 1:3, Fe amount: 0.75 g) was added to the PEI-SiO_2 solution under stirring conditions, forming a reddish-brown nitrogen-iron chelate, which was further sonicated for 8 hours to form a uniform and viscous complex solution. After being dried at 85 °C for 24 hours to remove water, the resulting

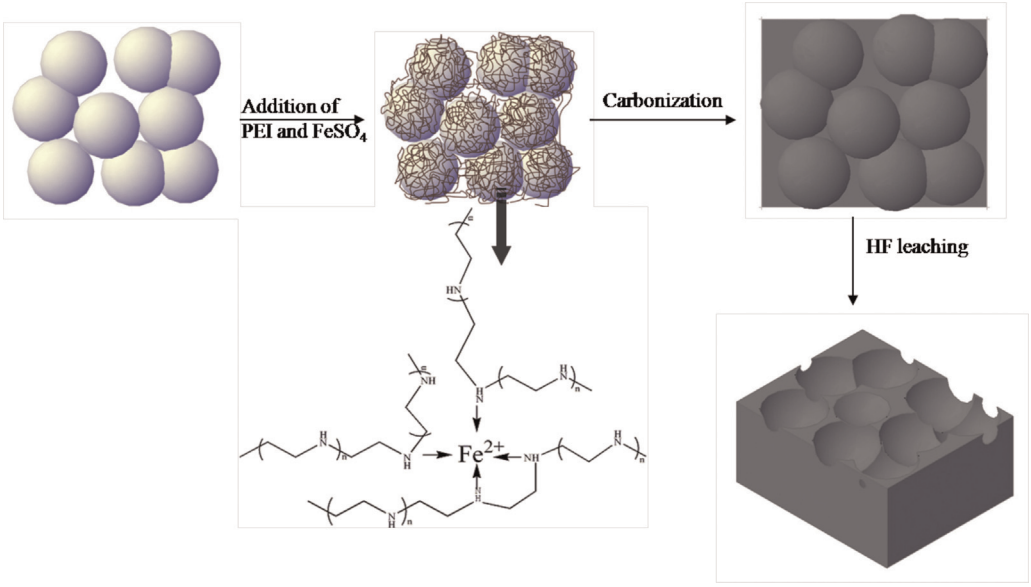

Fig. 1. Schematic of synthesis route of N and S co-doped mesoporous carbon materials by carbonization of $FeSO_4$-PEI-SiO_2 mixture, followed by etching of SiO_2 using HF.

solid was ground to a fine powder. The powder was then heat treated at 800 °C for 1 hour under a nitrogen atmosphere, with temperature ramp rates of 20 °C min^{-1}. The resulted black powder was denoted as $FeSO_4$-PEI-SiO_2. Finally, the SiO_2 was leached out using excess amounts of 40 wt.% hydrofluoric acid (HF) for 24 hours. The final powder was washed by deionized water to neutralize it, and dried overnight. The molecular structure of PEI, along with a schematic representation of the steps to prepare the $FeSO_4$-PEI catalyst, is illustrated in Fig. 1. For further improving the catalytic activity, the $FeSO_4$-PEI catalyst was post-treated with an acid-leaching step, using 0.5 M H_2SO_4 at 80 °C for 8 hours to form a sample denoted as $(FeSO_4\text{-PEI})_L$, which was re-pyrolyzed at 800 °C for 1 hour under a nitrogen atmosphere to form another catalyst, denoted as $(FeSO_4\text{-PEI})_{LH}$. To elucidate the synergetic effect between N and S, $Fe(CH_3COO)_2$ (abbreviate as $Fe(Ac)_2$) was used as the Fe-precursor instead of $Fe(SO_4)$ $7H_2O$ to prepare S-free counterparts, named $(Fe(Ac)_2\text{-PEI})_{LH}$. Meanwhile, samples without any metal precursor (named $(PEI)_{LH}$) prepared by the same procedure were also used as the reference, and a carbon-supported catalyst $(FeSO_4\text{-PEI/C})_{LH}$ was also prepared, using carbon black (Vulcan XC-72R) as the support.

2.2. Electrode preparation

To measure the catalytic activity of the above synthesized catalysts, 5 mg of each catalyst was successively suspended in a mixture containing 850 μL of water and isopropyl alcohol (Sinopharm Chemical Reagent Co., Ltd. 4:1), and 150 μL of Nafion® (DuPont, 0.5 wt.%) to form a catalyst ink, under sonication. Then 10 μL of this ink was twice applied onto a clean glassy carbon (GC) disk with a geometric area of 0.2475 cm^2 (5.6 mm diameter). The overall loading of the catalyst was 400 $\mu g\,cm^{-2}$ in respect of N and S doped carbon. The current densities reported here all use the geometric area of the carbon electrode.

2.3. Electrochemical measurements

The catalysts were tested for their electrocatalytic ORR activity in a glass cell consisting of three-electrodes in 0.5 M H_2SO_4 solution saturated in O_2 at room temperature. A platinum wire counter electrode and a saturated calomel reference electrode were used. All potentials in this work were reported versus the reversible hydrogen electrode (RHE). Prior to the ORR experiments, the electrolyte was deaerated by bubbling N_2 for at least 30 minutes for surface cyclic voltammetric measurements. RDE and RRDE techniques were used to perform electrochemical measurements using a Pine RDE instrument (Pine Research Instrumentation, USA). LSV curves were collected at a scan rate of 5 mV s^{-1} and a rotation rate of 1500 rpm within an electrode potential range of -0.1 ~ 0.9 V vs. RHE. RRDE measurements were used to monitor the formation of peroxide species during the ORR process catalyzed by the synthesized catalysts. The ring electrode (6.25 mm inner diameter and 7.92 mm outer diameter) collection efficiency was calibrated to be 0.37 using catalyst sample prepared in this work. The ring potential was fixed at 0.96 V vs. RHE to oxidize any possible peroxide produced during the potential scan of the disk electrode. All electrochemical experiments were carried out at room temperature and ambient pressure. For a comparison, 40 wt. % Pt/C (Johnson Matthey, JM) with a Pt loading of 32 $\mu g\,cm^{-2}$ was measured in 0.1 M $HClO_4$ solution.

2.4. Physical characterizations

The morphologies of various catalyst samples were characterized using a scanning electron microscope (HITACHI/S-4800). The microstructures were verified by XRD using a Rigaku D/max-2550 V diffractometer with Cu Kα radiation operating at 30 kV and 40 mA. The Brunauer-Emmett-Teller (BET) specific surface area and porosity of catalyst particles were characterized by nitrogen adsorption in a Micromeritics ASAP 2020 gas adsorption apparatus (USA). Surface analysis of the catalyst particles was carried out by XPS on a RBD upgraded PHI-5000C ECSA system (PerkinElmer) with Al K X-ray anode source ($h\nu$ = 1486.6 eV) at 14.0 kV and 250 W.

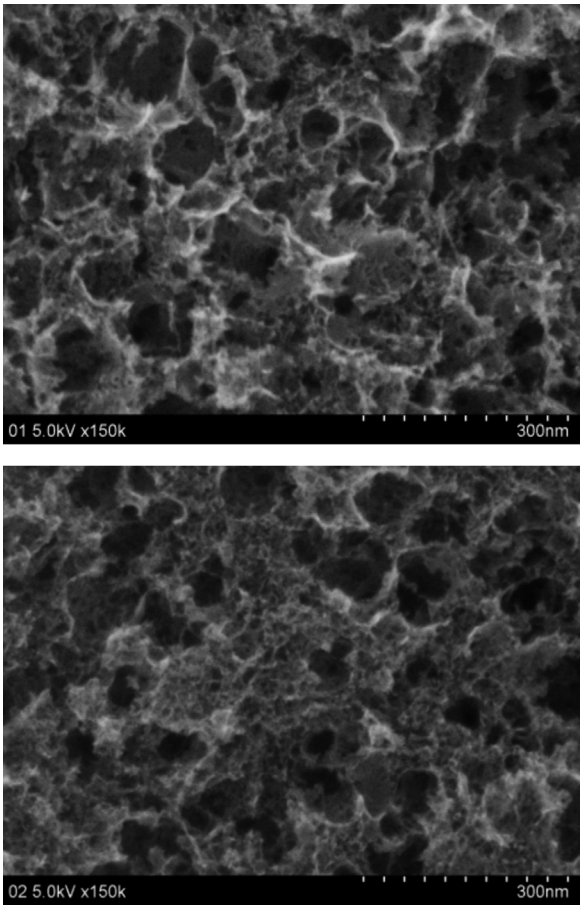

Fig. 2. SEM images for (a) $FeSO_4$-PEI and (b) $(FeSO_4\text{-PEI})_{LH}$ catalyst samples.

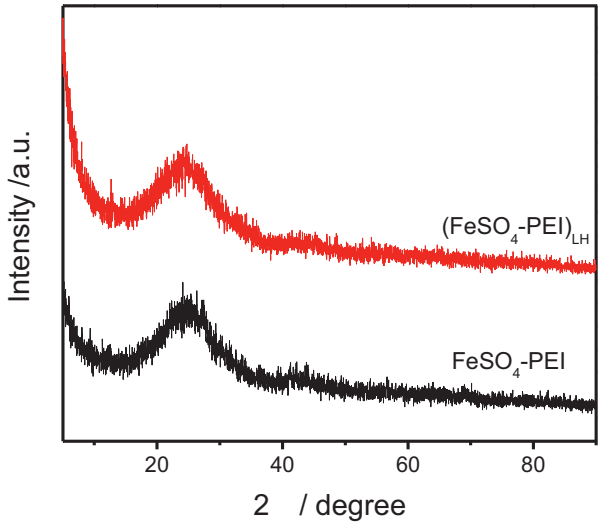

Fig. 3. XRD patterns for two $FeSO_4$-PEI catalysts before and after post-treatment.

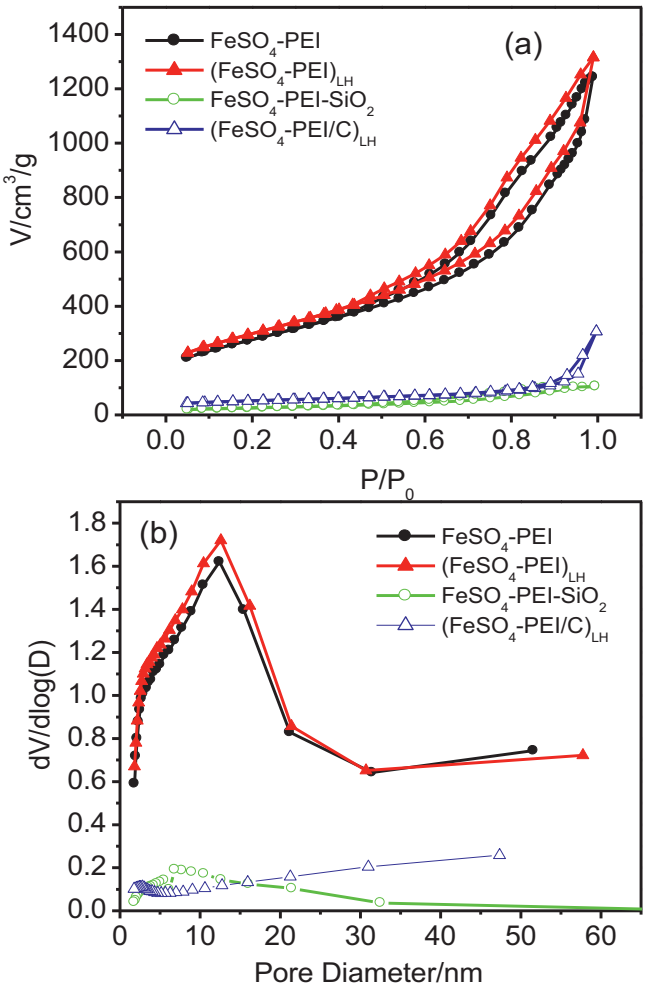

Fig. 4. (a) N_2 sorption isotherms of $FeSO_4$-PEI, $(FeSO_4\text{-PEI})_{LH}$, $FeSO_4$-PEI-SiO_2 and $(FeSO_4\text{-PEI/C})_{LH}$. (b) Pore size distribution, determined using the BJH method.

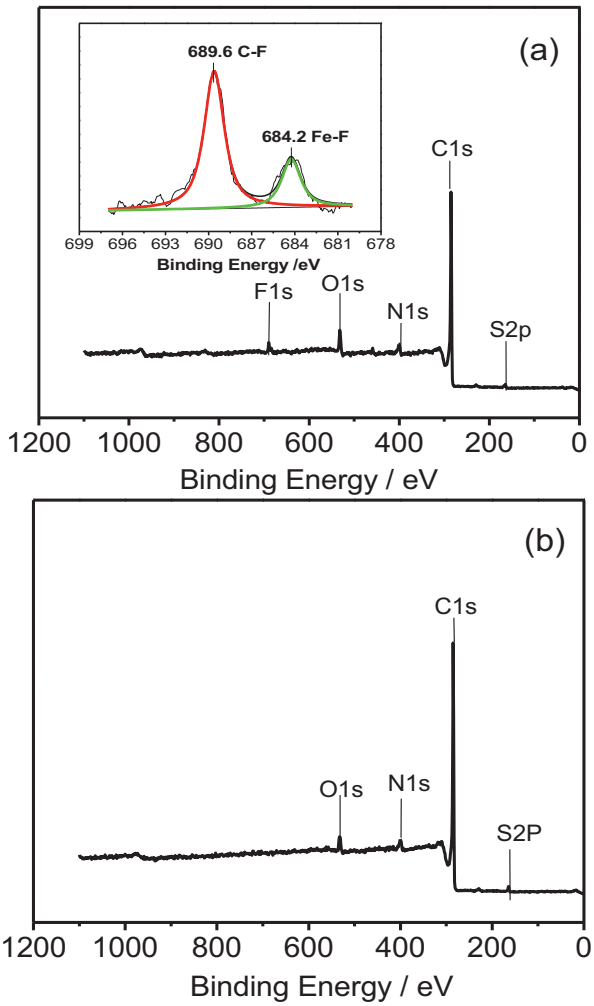

Fig. 5. XPS spectra of (a) $FeSO_4$-PEI and (b) $(FeSO_4\text{-PEI})_{LH}$ catalyst samples. The inset in (a) shows the F 1s XPS spectra for $FeSO_4$-PEI.

3. Results and discussion

3.1. Characterization of $FeSO_4$-PEI catalysts synthesized using different post-treatment methods

For physical characterizations, SEM was used first to characterize the morphologies of the carbon materials synthesized under different post-treatment conditions, as shown in Fig. 2. It can be seen that the disordered pores are cast successfully in the resultant carbon materials after different post-treatments, and both $FeSO_4$-PEI and $(FeSO_4\text{-PEI})_{LH}$ shows a sponge-like structure. It is noteworthy that there are some macropores with diameters at 50 – 100 nm on the surface of the $FeSO_4$-PEI samples. This may be formed by the vacation of stacked silica during HF etching (Fig. 2). Comparatively, the mesopores structures are not seen clearly from the SEM image. This is not surprising since the mesopores may be hidden by macropores, which cover the surface of catalyst as can be further verified by low N_2 absorption.

Fig. 3 shows the XRD patterns of samples that underwent different post-treatments. Only two broad diffraction peaks can be explicitly observed, at 23° and 43°, which correspond to the (002) and (004) planes of carbon materials with low graphitization, indicating a wholly amorphous structure. Obviously, this structure is consistent with the sponge-like structure shown in Fig. 2. No crystalline iron or iron oxide peak can be observed for either $FeSO_4$-PEI or $(FeSO_4\text{-PEI})_{LH}$, suggesting the complete removal of crystalline iron and iron oxide from the catalyst subjected to leaching with HF. However, lack of crystalline iron or iron oxide peaks may not guarantee complete removal of iron. Traces of Fe may still be bonded in amorphous forms and this will be discussed further by following ICP results.

The textural properties of $FeSO_4$-PEI, $(FeSO_4\text{-PEI})_{LH}$, $FeSO_4$-PEI-SiO_2 and $(FeSO_4\text{-PEI/C})_{LH}$ were investigated using low-temperature nitrogen adsorption, and the results are shown in Fig. 4. It can be seen that the nitrogen adsorption/desorption isotherms of $FeSO_4$-PEI and $(FeSO_4\text{-PEI})_{LH}$ belong to the type IV with H3 loop isotherms, according to IUPAC classification, exhibiting a distinct hysteresis loop in the medium- and high-pressure regions ($P/P_0 = 0.45 \sim 1$). $FeSO_4$-PEI and $(FeSO_4\text{-PEI})_{LH}$ both show high BET surface areas, reaching 986 and 1064 $m^2\,g^{-1}$, respectively, which are much higher than that of $FeSO_4$-PEI-SiO_2 (91 $m^2\,g^{-1}$) and $(FeSO_4\text{-PEI/C})_{LH}$ (176 $m^2\,g^{-1}$). As expected, the mesoporous size distribution is centered at 12 nm both for $FeSO_4$-PEI and $(FeSO_4\text{-PEI})_{LH}$, according to calculation using the Barrett-Joyer-Halenda (BJH) method. This value is in agreement with the size of the template silica nanoparticles. However, for $FeSO_4$-PEI-SiO_2 and $(FeSO_4\text{-PEI/C})_{LH}$, no mesopores with centered diameter were observed, indicating that all the synthesized $FeSO_4$-PEI catalyst samples inherits the spherical morphology of the silica template. Besides the mesopores, a small amount of macropores with diameter larger than 50 nm can also be observed in both $FeSO_4$-PEI and $(FeSO_4\text{-PEI})_{LH}$ samples. Compared to the sample that did not undergo post-treatment, fewer macropores

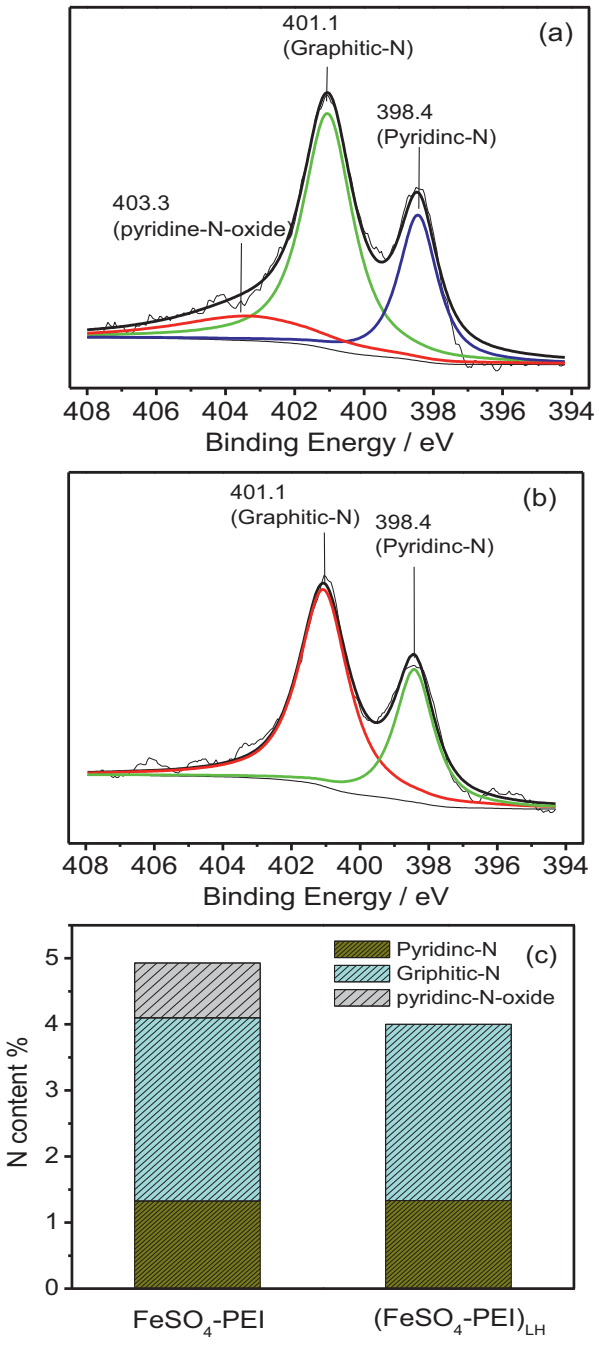

Fig. 6. High-resolution N 1s XPS spectra of (a) $FeSO_4$-PEI and (b) $(FeSO_4\text{-PEI})_{LH}$. (c) Percentage content of three types of N in the samples.

and more mesopores are in evidence after H_2SO_4 leaching and reheating. Moreover, there are also some micropores in these catalysts according to the calculation of Horvath- Kawazoe. The cumulative micropore volume is 0.28, 0.27 and 0.31 $cm^3\,g^{-1}$ for $FeSO_4$-PEI, $(FeSO_4\text{-PEI})_L$ and $(FeSO_4\text{-PEI})_{LH}$ respectively. This may comes from the contribution that the thin walls of the macropores are damaged by acid leaching and reheating, thus the pores shrink. As will be verified by XPS results later, the removal of impurities by H_2SO_4 leaching, and further volatilization of some small molecules (NO_X, NH_3, SO_X, H_2S, CO_2, CH_X, etc.) during the reheating treatment, could also have contribution to the increased number of smaller pores. Combining what will be discussed later, the shrink of macropores, removal of impurities and loss of N and S by post-treatment might make contribution to the increased BET surface area of $(FeSO_4\text{-PEI})_{LH}$.

Normally, carbon with bimodal or trimodal porosity is of great practical interest. On the one hand, the macropores can serve as a buffering reservoir of electrolyte, shortening the diffusion distance to the interior surfaces [30]. On the other hand, the mesopores or microspores can provide a large surface area and expose more ORR-relevant active sites; they can also play an important role in mass transfer, thus facilitating the ORR kinetics and preventing water flooding. As can be seen in Fig. 4, despite slight differences in the BET surface areas and pore structures of the two samples, both $FeSO_4$-PEI and $(FeSO_4\text{-PEI})_{LH}$ show much higher BET surface areas than conventional catalysts supported on Vulcan XC-72R, and have appropriate pore structures, suggesting that high ORR performance will be promoted by these morphological factors.

Fig. 5 shows the results of XPS analysis, employed to study the surface chemical composition of the samples before and after acid leaching and reheating. It can be seen that N and S are both present in the samples, demonstrating that N and S were successfully doped into $FeSO_4$-PEI and $(FeSO_4\text{-PEI})_{LH}$ by pyrolyzing the PEI and ferrous sulfate mixture without needing to add extra N or S sources. It has been reported that doping carbon with heteroatoms may not only create more defects, but also lead to deformation of the carbon (open edge sites, high curvature), thus resulting in a sponge-like carbon structure [26]. Therefore, the presence of N and S may contribute to the high BET surface area of the two samples partly. While it can't explain why $(FeSO_4\text{-PEI})_{LH}$ (with less N and less S than $FeSO_4$-PEI) has higher BET surface area, combining with the increase of micropore volume discussed above, it is reasonable to deduce that the loss of N and S during re-pyrolysis may create more micropores and make contribution to the higher BET surface area of $(FeSO_4\text{-PEI})_{LH}$.

As expected, no iron spectra could be found in the wide-scan spectra of the $(FeSO_4\text{-PEI})_{LH}$. This may demonstrate that the iron compounds on the catalyst surface were removed during the HF and H_2SO_4 leaching, which is in a well agreement with the XRD results (Fig. 3). However, further by elemental analysis using ICP technique, the final metal content of catalysts was found to be 0.2 ~ 0.3 wt.% both for $FeSO_4$-PEI and $(FeSO_4\text{-PEI})_{LH}$. According to the literatures most recently reported [31,32], even a slight trace of metallic impurities in carbon materials may have a strong influence on the ORR. Therefore, we could not completely rule out the contribution of residual Fe to the ORR performance in this work, although the content of Fe is very small.

Interestingly, the $FeSO_4$-PEI sample shows five peaks, associated with C, N, O, S and F (Fig. 5(a)), while $(FeSO_4\text{-PEI})_{LH}$ shows only four, the F 1s peak being absent (Fig. 5(b)). A high-resolution view

Table 1
XPS Results of $FeSO_4$-PEI and $(FeSO_4\text{-PEI})_{LH}$

Catalysts	Total surface N content (at.%)	Surface content (at. %) of different N functionalities			Total surface S content (at.%)	Surface content (at. %) of different S functionalities		
		N1	N2	N3		S1	S2	S3
$FeSO_4$-PEI	4.93	1.39	2.94	0.60	1.20	0.46	0.27	0.47
$(FeSO_4\text{-PEI})_{LH}$	4.00	1.39	2.61	–	0.83	0.41	0.29	0.13

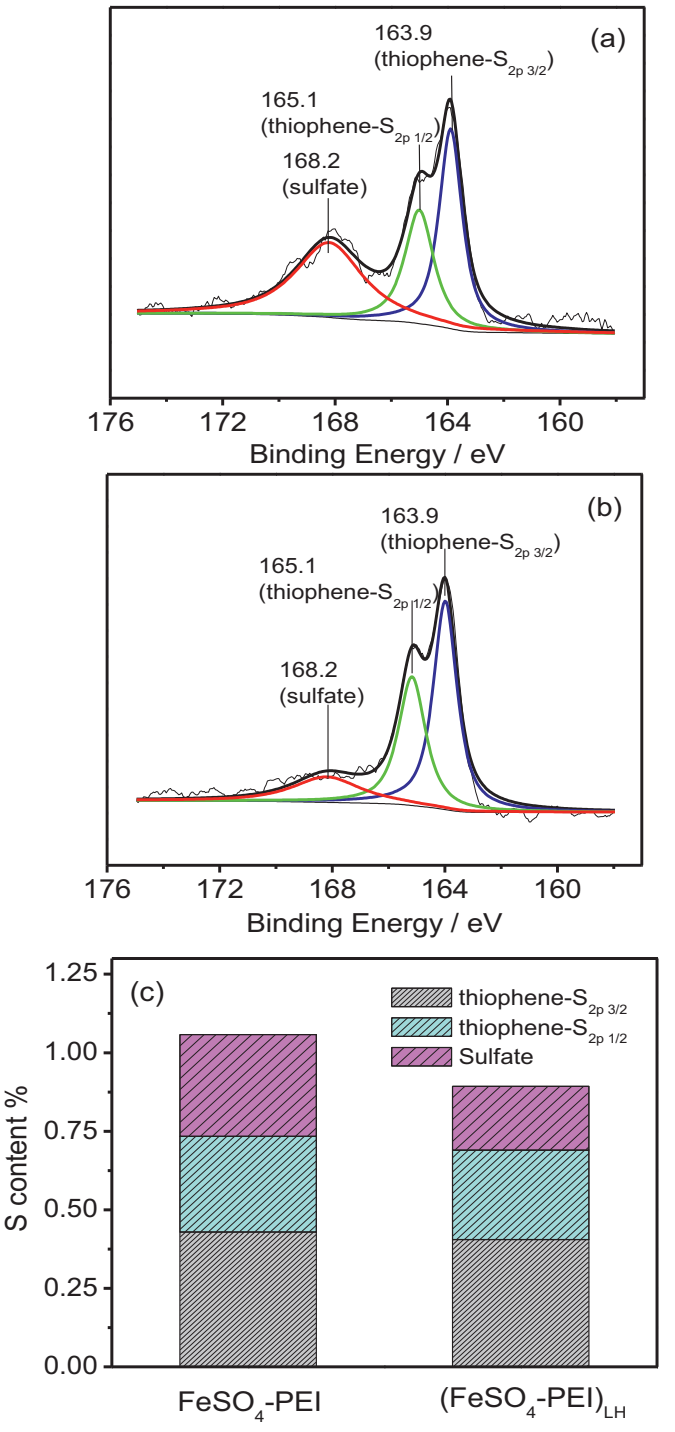

Fig. 7. High-resolution S 2p XPS spectra of (a) $FeSO_4$-PEI and (b) $(FeSO_4\text{-PEI})_{LH}$. (c) Percentage content of three types of sulfur in the samples.

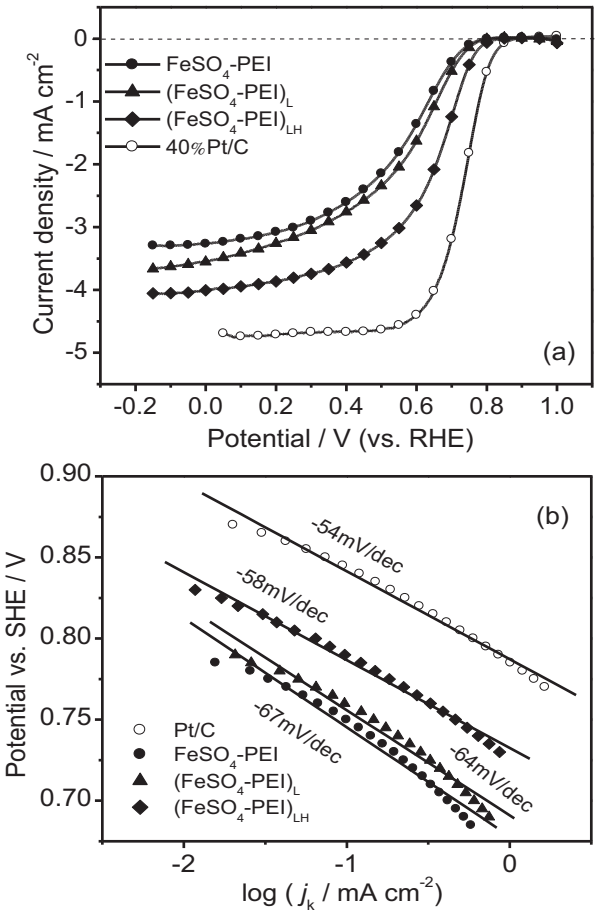

Fig. 8. (a) Polarization curves on RDE for $FeSO_4$-PEI catalysts synthesized under different post-treatments and Pt/C at a scan rate of 5 mV s^{-1} in O_2-saturated 0.5H_2SO_4 solution (0.1 M $HClO_4$ for Pt/C); (b) Tafel plots of log i_k vs. E (V) for the ORR on $FeSO_4$-PEI catalysts using different post-treatments, deduced from the polarization curves in (a). Catalyst loading: 400 μg cm^{-2}; rotation rate: 1500 rpm.

of the F1s spectra (see the inset graph in Fig. 5(a)) shows that there are two main F1s peaks for the $FeSO_4$-PEI sample. The first component at 687.5 eV is related to a C-F covalent bond. The second component, at 684.2 eV, originates from an ionic-F bond [33,34], which is attributed to iron fluoride produced in the process of HF leaching. After acid leaching by H_2SO_4 and reheating, the covalent and ionic bonds disappear as shown in Fig. 5(b). This reveals that acid leaching and reheating play important roles in removing impurities and purifying the active sites.

It is expected that doping nitrogen into the carbon structure may play a significant role in ORR catalytic activity. On the basis of this conception, the high resolution N 1s spectra for the two samples are presented in Fig. 6. The calculated atomic percentages of different N and S functionalities in the prepared materials are given in Table 1. The results reveal that 4.93 and 4.00 at.% nitrogen were introduced into $FeSO_4$-PEI and $(FeSO_4\text{-PEI})_{LH}$, respectively. The decrease N content in $(FeSO_4\text{-PEI})_{LH}$ may be due to the further volatilization of N-containing small molecules (NO_X, NH_X, etc.) as discussed previously. In the $FeSO_4$-PEI sample, N is doped into the carbon lattice as pyridinic-N (N1, 398.4 eV), graphitic-N (N2, 401.1 eV) and pyridinc-N-oxide (N3, 403.3 eV) (Fig. 6(a)), which are commonly observed in N-doped carbons [35–37]. After acid leaching and reheating, pyridine-N-oxide, which is considered a catalytically inactive species for the ORR, almost disappears, and pyridinic-N and graphitic-N keep all the nitrogen (Fig. 6(b)). In addition, the content of stable pyridinic-N and graphitic-N, which have been reported as active sites of ORR, almost remain the same in $FeSO_4$-PEI and $(FeSO_4\text{-PEI})_{LH}$. This, along with the fact that the ORR performance of $(FeSO_4\text{-PEI})_{LH}$ is much higher than that of $FeSO_4$-PEI as we will discussed in the next section, brings us to conclude that the disappearance of unstable pyridine-N-oxides may expose more active sites for electrocatalysis.

Fig. 7 shows the high-resolution spectra of S 2p. After H_2SO_4 leaching and reheating treatment, the S content decreases from 1.20 to 0.83 at.%, which can be attribute to the further volatilization of S-containing small molecules (SO_X, H_2S etc.). The $FeSO_4$-PEI sample shows a large band at 168.2 eV(S3), which may be assigned to the sulfate in the catalyst precursor. The other two peaks of S 2p

Table 2
Parameters for ORR on $FeSO_4$-PEI catalysts synthesized under different post-treatments and Pt/C catalyst.

Catalyst	Onset potential (V)[a]	Half-wave potential (V)[a]	i_k at 0.7 V (mA cm^{-2})[a]
$FeSO_4$-PEI	0.750	0.600	0.30
$(FeSO_4\text{-PEI})_L$	0.760	0.620	0.40
$(FeSO_4\text{-PEI})_{LH}$	0.790	0.680	1.35
Pt/C	0.840	0.736	1.85

[a] : Conditions: O_2-saturated 0.5 M H_2SO_4, 1500 rpm, 5 mV s^{-1}, catalyst loading 400 μg cm^{-2}. The onset potential was defined at a specific current density at 0.1 mA cm^{-2}.

in $FeSO_4$-PEI are in agreement with the reported $S_{2p3/2}$ (S1, 163.9 eV) and $S_{2p1/2}$ (S2, 165.1 eV) positions of thiophene-S owing to their spin-orbit coupling [29]. Just as N functionalities, there is no significant change in the content of thiophene-S—reportedly the active site for the ORR [38], however, the inactive species—sulfate band shrinks sharply. The above results demonstrated further that due to the decrease of inactive species (both pyridine-N-oxide and sulfate in this work), more ORR-relevant active sites would be exposed, which leads to these purified active sites (pyridinic-N, graphitic-N and thiophene-S) contribute to the highly improved ORR performance.

3.2. Electrocatalysis of the ORR on $FeSO_4$-PEI catalysts synthesized using different post-treatments

Fig. 8 (a) shows the polarization curves for the ORR in O_2-saturated 0.5 M H_2SO_4 solution on GC electrodes coated with $FeSO_4$-PEI catalysts synthesized under different post-treatments. When a voltage is applied, besides ORR, two layers of ions with opposing polarity will form at the interface boundary between a conductive electrode and an adjacent liquid electrolyte, resulting in the capacitive current. Therefore, we got the pure ORR current when we deduct current measured in N_2-saturated electrolyte from current measured in O_2-saturated electrolyte. For a good comparison, LSV curves of Pt/C in 0.1 M $HClO_4$ is also presented in the same figure. For clarity, the onset potential (determined as the potential at 0.1 mA cm^{-2}), half-wave potential, and catalytic current density (i_k) at 0.7 V are summarized in Table 2. As can be seen from Fig. 8(a) and Table 1, the $FeSO_4$-PEI catalyst shows high ORR activity with a half-wave potential at 0.60 V. From what has been discussed by N_2 adsorption and XPS, obviously the relatively high BET surface area, proper pore structure, and purified ORR-relevant active sites of $FeSO_4$-PEI (including pyridinc-N, graphitic-N and thiophene-S) may lead to its high ORR activity. After acid leaching with 0.5 M H_2SO_4, the ORR activity increases, indicated by the ~ 20 mV positive shift in the half-wave potential. Very interestingly, after the catalyst is reheated, the ORR activity increases significantly again, with the half-wave potential reaching 0.68 V vs. SHE and deviating only ~56 mV from that of the Pt/C catalyst. In addition, the diffusion-limiting current of $(FeSO_4\text{-PEI})_{LH}$ is also much higher (one-third greater) than that of both $FeSO_4$-PEI and $(FeSO_4\text{-PEI})_L$, suggesting that reheating after H_2SO_4 leaching may be an effective way to achieve the most electroactive catalyst. It should be noteworthy that result of our work showed much higher ORR performance than those reported elsewhere [27,39–42], which showed a reasonable ORR activity in alkaline electrolytes, but a poor activity in acidic solutions.

The slope of the ORR Tafel plot can further clarify our understanding of how different catalyst electrodes alter the ORR kinetics. Such alterations can reflect changes in the ORR mechanism. Fig. 8 (b) presents the Tafel plots of log i_k (mA cm^{-2}) vs. the electrode potential E, deduced from the polarization curves of Fig. 8 (a) recorded at an electrode rotation rate of 1500 rpm. The kinetic current density, i_k, is estimated by correcting the mass transport according to Equation (1):

$$i_k = \frac{i_l i}{i_l - i} \quad (1)$$

where i_l is the limiting current density, and i is the measured current density. In general, the Tafel slope for an ORR catalyst can be divided into two parts: (i) the low current density region (low overpotentials) and (ii) the high current density region (high overpotentials). In the low current density region, the disk current density (i_d) for the ORR is almost independent of the electrode rotation rate, suggesting that the current densities in this narrow potential range are purely electrochemical kinetic current densities [43]. Therefore, the activity differences for the $FeSO_4$-PEI catalysts subjected to different post-treatments can be clearly identified from the Tafel plots in the low current density region. For $FeSO_4$-PEI, the Tafel slope is around −67 mV dec^{-1} at the low overpotential region. The Tafel slope decreases to −64 mV dec^{-1} for $(FeSO_4\text{-PEI})_L$ after the sample undergoes acid leaching, then drops further to −58 mV dec^{-1} for $(FeSO_4\text{-PEI})_{LH}$ after the sample is further treated by pyrolysis. Similar to ORR catalyzed by platinum, the Tafel slope of $(FeSO_4\text{-PEI})_{LH}$ approached to theoretical calculating value ($-2.303RT/\alpha F \approx 60$ mV per decade) at room temperature, indicating that transfer of the first electron is probably the rate-determining step [44]. These data clearly indicate that the ORR mechanism strongly depends on the different post-treatment(s).

For a good comparison, electrocatalytic activities of $(FeSO_4\text{-PEI/C})_{LH}$ and $FeSO_4$-PEI-SiO_2 are presented in Fig. 9. It can be seen that $(FeSO_4\text{-PEI})_{LH}$ shows much higher electrocatalytic activity than $(FeSO_4\text{-PEI/C})_{LH}$ and $FeSO_4$-PEI-SiO_2 in terms of both onset potential and half-wave potential. This demonstrates that high BET surface area and suitable pores of $(FeSO_4\text{-PEI})_{LH}$ can play an important role in facilitating ORR electrocatalytic activities. Moreover, LSV curves of $(PEI)_{LH}$ and $(Fe(Ac)_2\text{-PEI})_{LH}$ are also presented in Fig. 9 to verify the S-doped effect. Even higher

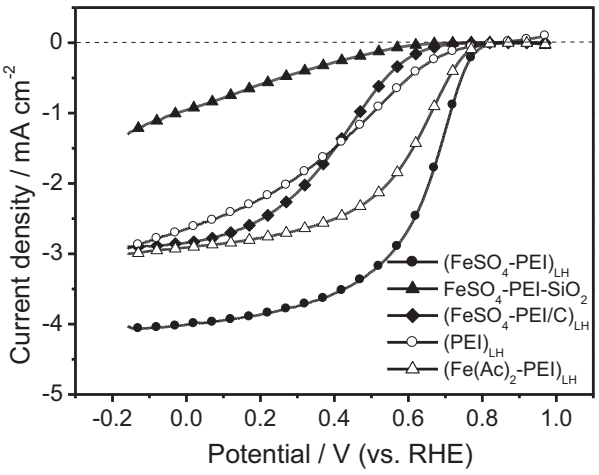

Fig. 9. Polarization curves on RDE for $(FeSO_4\text{-PEI})_{LH}$, $FeSO_4$-PEI-SiO_2, $(FeSO_4\text{-PEI/C})_{LH}$, $(PEI)_{LH}$ and $(Fe(Ac)_2\text{-PEI})_{LH}$ at a scan rate of 5 mV s^{-1} in O_2-saturated 0.5H_2SO_4 solution; Catalyst loading: 400 μg cm^{-2}; rotation rate: 1500 rpm.

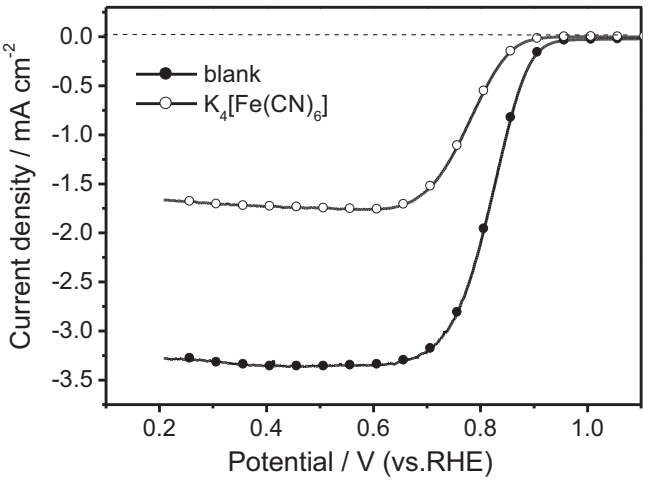

Fig. 10. RDE measurements of the oxygen reduction activity of $(FeSO_4\text{-}PEI)_{LH}$ in O_2-saturated 0.1 M NaOH and 0.1 M NaOH + 10 mM $K_4[Fe(CN)_6]$. Data were recorded at 1500 rpm and 5 mV s^{-1} (current measured in N_2-saturated electrolyte has been subtracted as background value).

nitrogen content (4.93 at.%) is introduced in, $(PEI)_{LH}$ shows poorer ORR performance than $(FeSO_4\text{-}PEI)_{LH}$, about 240 mV negatively in regarding of half-wave potential. This demonstrates that pyrolysis of PEI in the presence of $FeSO_4$ can improve ORR performance significantly. Moreover, it was found that the ORR half-wave potential on $(Fe(Ac)_2\text{-}PEI)_{LH}$ (N content 5.95 at.%) was 40 mV lower than that for the $(FeSO_4\text{-}PEI)_{LH}$ synthesized using $FeSO_4$ as the Fe-precursor, indicating the presence of S could benefit the ORR activity.

To further clarify the influence of the trace amount of Fe, the ORR activity of $(FeSO_4\text{-}PEI)_{LH}$ was evaluated in the presence of potassium hexacyanoferrate ($K_4[Fe(CN)_6]$) because cyanide is known to form very strong complexes with iron and poison the ORR at iron centers [45,46]. Fig. 10 shows the RDE measurements of the oxygen reduction activity of $(FeSO_4\text{-}PEI)_{LH}$ in 0.1 M NaOH with and without the addition of 10 mM $K_4[Fe(CN)_6]$ (current measured in N_2-saturated electrolyte has been subtracted as background value to exclude the effect of capacitive current and oxidation-reduction reaction of and Fe^{2+}). It can be seen that in the presence of $K_4[Fe(CN)_6]$, the onset potential of catalyst negatively shifted by ~100 mV, and the diffusion-limited current density fell almost by half. Therefore, it can be concluded that in this catalyst, trace metal is a part of the constitution of active sites and plays an important role in facilitating oxygen reduction. Combined the verified N and S-doped and trace metal effect, it can be inferred that the synergetic coupling effect of the Fe + N + S combinations may lead to the high ORR performance of the series of catalysts.

Considering all the above characterizations and analyses, it can be reasonably concluded that H_2SO_4 leaching and reheating processes can remove ORR inactive impurities, such as C-F, Fe-F, pyridinc-N-oxide, and sulfate as shown in Figs. 5–7, leading to more ORR active sites available such as pyridinc-N, graphitic-N and thiophene-S. This may be one of the explanations for the enhanced ORR performance of $(FeSO_4\text{-}PEI)_{LH}$ (see Figs. 8 and 9). Moreover, the uniform, dense mesopores and higher BET surface area of $(FeSO_4\text{-}PEI)_{LH}$ can help the electron and reactant transfer during the catalyzed ORR process. Therefore, the synergetic effect of purified active sites, along with the modified carbon matrix arising from H_2SO_4 leaching and reheating, may contribute to the catalysts' enhanced ORR activity.

Normally, to evaluate a NPM catalyst, two key performance parameters have to be considered: activity comparable to the platinum benchmark, and sufficiently high durability. One of

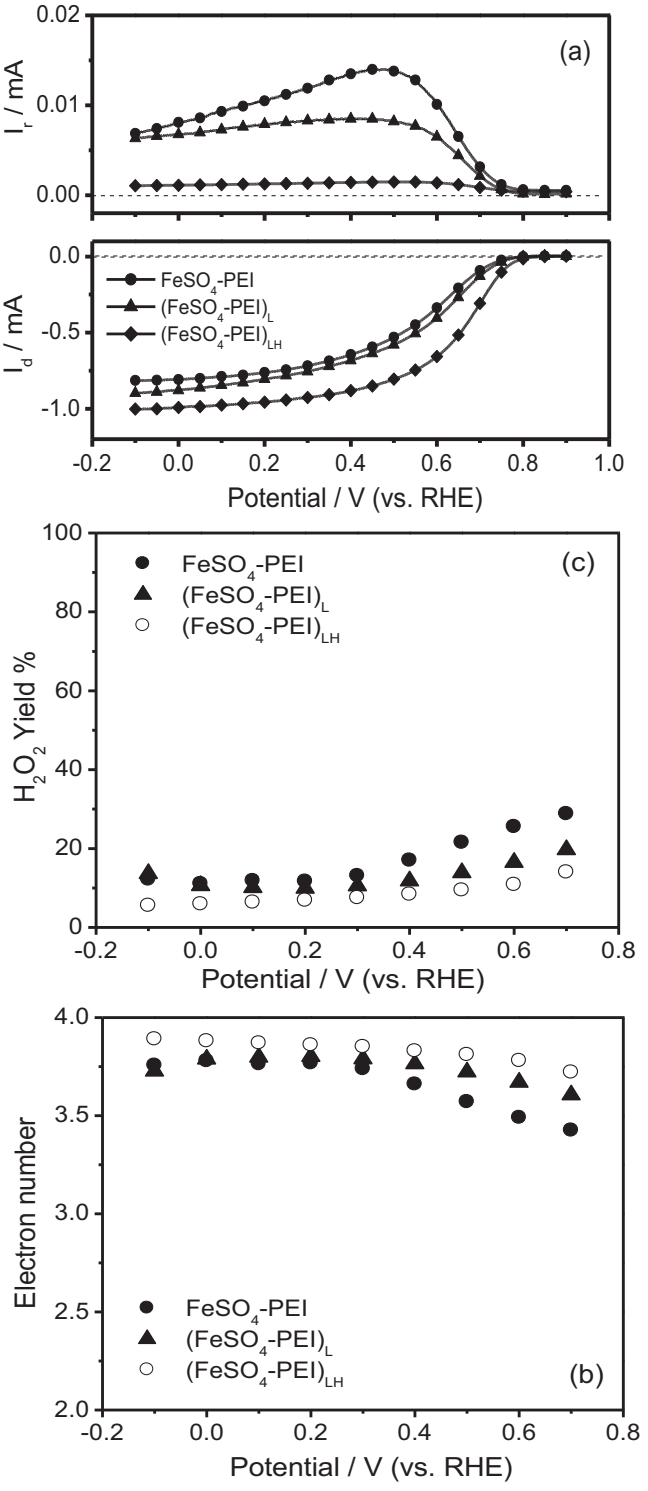

Fig. 11. (a) RRDE measurements for oxygen reduction on $FeSO_4$-PEI catalysts synthesized using different post-treatments at a scan rate of 5 mV s^{-1} in O_2-saturated 0.5H_2SO_4 solution; (b) the corresponding percentage of H_2O_2 produced; and (c) the electron transfer numbers of the corresponding samples. Catalyst loading: 400 $\mu g\,cm^{-2}$; rotation rate: 1500 rpm.

the problems typically plaguing NPM cathode catalysts is their high hydrogen peroxide generation (H_2O_2), which is the result of the $(2\times2)e^-$ mechanism and lead to severe corrosion of the carbonaceous catalyst, and even of the membrane and ionomer [47]. For a more quantitative evaluation, the number of electrons transferred and the percentage of H_2O_2 produced during the ORR

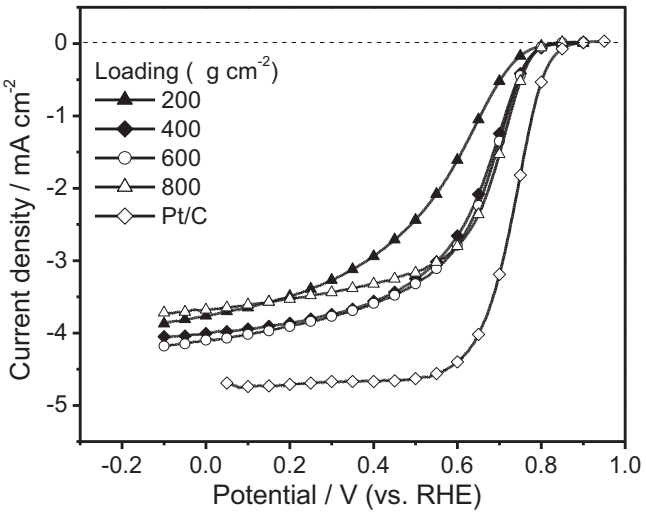

Fig. 12. Polarization curves on RDE for $(FeSO_4\text{-}PEI)_{LH}$ catalyst with different loadings at a scan of 5 mV s^{-1} in O_2-saturated 0.5H_2SO_4 solution; Pt/C in 0.1 M $HClO_4$ for comparison. Rotation rate: 1500 rpm.

process catalyzed by $FeSO_4$-PEI catalysts synthesized using different post-treatment method can be investigated using the RRDE technique and calculated using Equations (2) and (3), respectively:

$$n = \frac{4I_d}{I_d + I_r/N} \tag{2}$$

$$\%H_2O_2 = 100 \times \frac{2I_r/N}{I_d + I_r/N} \tag{3}$$

where I_d, I_r, and N are the disk current, ring current and collection efficiency (0.37), respectively. It was found in all cases that $FeSO_4$-PEI, $(FeSO_4\text{-}PEI)_L$ and $(FeSO_4\text{-}PEI)_{LH}$ are H_2O_2 inhibiters, yielding less than 28% H_2O_2. Fig. 11 (a) reveals that H_2O_2 released into the electrolyte decreases with further post-treatment. The H_2O_2 yield percentage was in the range of 15 ~ 28%, 10 ~ 20% and 5 ~ 12% in the potential range of–0.1 ~ 0.7 V for $FeSO_4$-PEI, $(FeSO_4\text{-}PEI)_L$ and $(FeSO_4\text{-}PEI)_{LH}$ catalysts, respectively. The low H_2O_2 yield renders $(FeSO_4\text{-}PEI)_{LH}$ more stable for long-running processes with a low risk of deactivation. Accordingly, the number of electrons was calculated to be 3.45 ~ 3.75, 3.62 ~ 3.80 and 3.76 ~ 3.90 in the same potential range for $FeSO_4$-PEI, $(FeSO_4\text{-}PEI)_L$ and $(FeSO_4\text{-}PEI)_{LH}$, respectively, indicating that in acid electrolyte they catalyze the ORR mainly via a four-electron pathway. This is consistent with heteroatom-doped catalysts reported by other groups [42,48,49].

Although the $(FeSO_4\text{-}PEI)_{LH}$ catalyst shows high ORR performance, it is still barely satisfying as a replacement for commercial Pt/C. Given the catalyst's low cost, increasing the loading of $(FeSO_4\text{-}PEI)_{LH}$ to reach a desirable ORR performance is practicable. Fig. 12 shows the disk current for the $(FeSO_4\text{-}PEI)_{LH}$ catalyst with loadings ranging from 200 ~ 800 $\mu g\,cm^{-2}$. It can be seen that for the electrode with low catalyst loading (200 $\mu g\,cm^{-2}$), the ORR activity is very low and no well-defined limiting plateau can be observed. However, when the catalyst loading is increased to higher than 200 $\mu g\,cm^{-2}$, both onset potential and half-wave potential are greatly improved, and a comparatively well-defined mass-transfer-limited current plateau appears. What deserves to be noticed here is that the half-wave potential of the electrode with a loading of 800 $\mu g\,cm^{-2}$ reaches 0.7 V, which is only ~36 mV deviation from Pt/C catalyst at a loading of 32 μg (Pt) cm^{-2}. It is noteworthy that the limiting current of the electrode undergoes no obvious change with catalyst loadings ranging from 400 ~ 600 $\mu g\,cm^{-2}$, and even

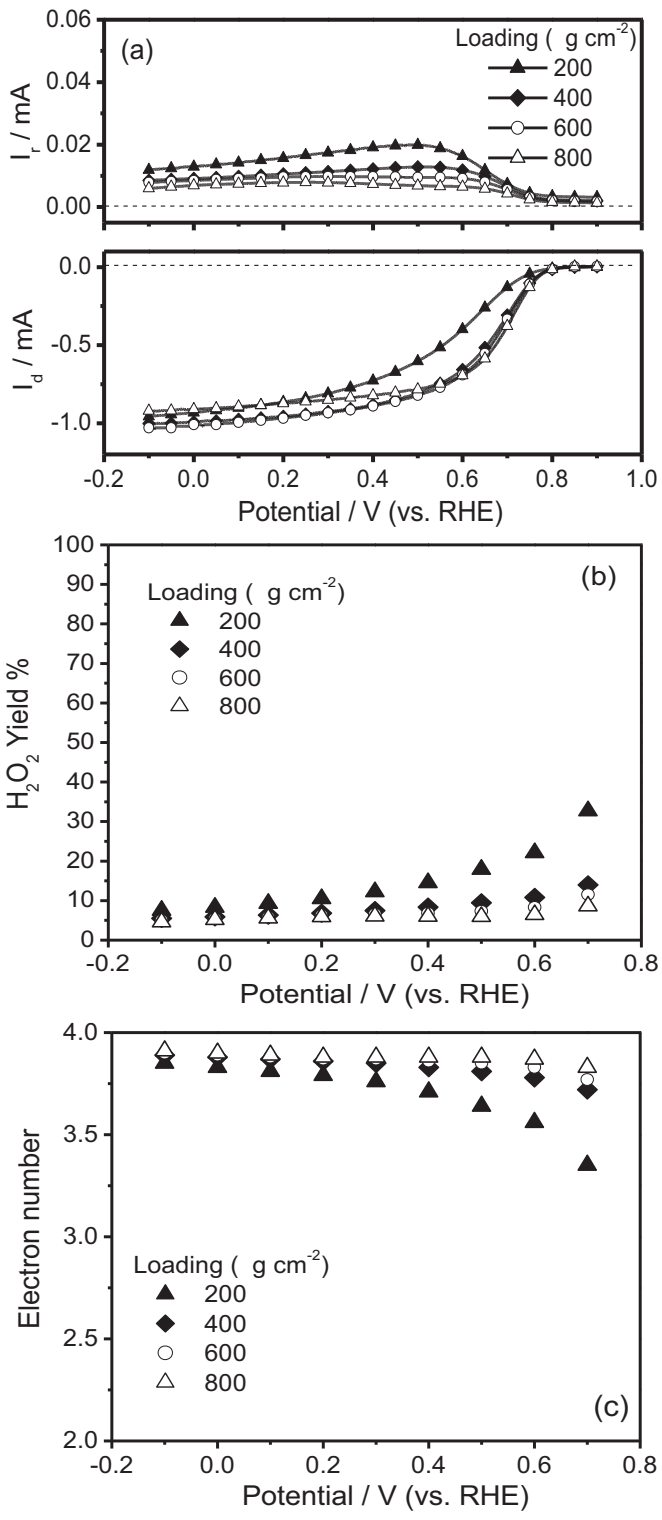

Fig. 13. (a) RRDE measurements for $(FeSO_4\text{-}PEI)_{LH}$ catalyst with different loadings at a scan rate of 5 mV s^{-1} in O_2-saturated 0.5H_2SO_4 solution; (b) the corresponding percentage of H_2O_2 produced; and (c) the electron transfer numbers of the corresponding samples. Rotation rate: 1500 rpm.

decreased at highest loading (800 $\mu g cm^{-2}$). This may due to the fact that thickening of the Nafion layer, caused by increased loading, can hamper the mass transfer of ORR-relevant species (H^+, e^-, O_2, OH^- and H_2O).

To obtain insight into the effect of loading on the ORR mechanism catalyzed by $(FeSO_4\text{-}PEI)_{LH}$, further RRDE

measurements were conducted (Fig. 13(a)). The electron number and percentage of H_2O_2 produced during the ORR process at different loadings are displayed in Fig. 13(b) and (c). It can be seen that the number of electrons transferred over a potential range of–0.1 ~ 0.7 V increases with increasing catalyst loading, reaching almost 4 for the highest loading (800 $\mu g\,cm^{-2}$) (Fig. 13(b)). Accordingly, Fig. 13(a) and (c) show that the greater the loading coated on the electrode, the lower the percentage of H_2O_2 produced. In particular, for the highest loading of 800 $\mu g\,cm^{-2}$, less than 8% H_2O_2 is produced. Obviously, the high number of active sites introduced by high loading can transform H_2O_2 (which is produced in the thick catalyst layer) into H_2O, resulting in an apparently lower H_2O_2 percentage and a higher electron number. Even at the lowest loading of 200 $\mu g\,cm^{-2}$, the electron transfer number at 0.4 V are still larger than 3.6, suggesting an intrinsic four-electron-transfer process of $(FeSO_4\text{-}PEI)_{LH}$ catalyst in this work [50].

4. Conclusions

In this work, N and S co-doped mesoporous-structured, high-surface-area carbon electrocatalysts, expressed as $FeSO_4$-PEI, $(FeSO_4\text{-}PEI)_L$ and $(FeSO_4\text{-}PEI)_{LH}$, are successfully synthesized by simple pyrolysis of a $FeSO_4$-PEI-SiO_2 mixture at high temperature and removal of the SiO_2 template using HF. The effect of post-treatments, including H_2SO_4 leaching and reheating, are investigated using XRD, SEM, low-temperature N_2 adsorption, XPS and ICP. All samples show strong catalytic activities toward the ORR in acidic solution. Of the three catalysts, $(FeSO_4\text{-}PEI)_{LH}$ shows the largest BET surface area of 1064 $m^2\,g^{-1}$, giving the highest ORR activity (half-wave potential 0.68 V) and selectivity (electron transfer number > 3.76). Moreover, increasing the catalyst loading can effectively improve the ORR activity; the electrode coated with a high loading of 800 $\mu g\,cm^{-2}$ exhibits only ~36 mV deviation from commercial Pt/C catalyst. The synergetic coupling effect of the Fe + N + S combinations may lead to the high ORR performance of the series of catalysts. The observed superior ORR performance of $(FeSO_4\text{-}PEI)_{LH}$ may be caused by purified active sites such as pyridinc-N, graphitic-N and thiophene-S, and the carbon matrix structure modified by H_2SO_4 leaching and reheating.

Acknowledgements

This work was supported by the National Natural Science Foundation of China (21173039); the Specialized Research Fund for the Doctoral Program of Higher Education, SRFD (20110075110001) of China; the Innovation Program of the Shanghai Municipal Education Commission (14ZZ074); International Academic Cooperation and Exchange Program of Shanghai Science and Technology Committee (14520721900), the Graduate Thesis Innovation Fundation of Donghua University (EG2014015) and College of Environmental Science and Engineering, State Environmental Protection Engineering Center for Pollution Treatment and Control in Textile Industry, Donghua University, Shanghai 201620, China. All the financial supports are gratefully acknowledged.

References

[1] Z.W. Chen, D.C. Higgins, A.P. Yu, L. Zhang, J.J. Zhang, A review on non-precious metal electrocatalysts for PEM fuel cells, Energy Environ. Sci. 4 (2011) 3167.
[2] M. Lefèvre, E. Proietti, F. Jaouen, J.P. Dodelet, Iron-based catalysts with improved oxygen reduction activity in polymer electrolyte fuel cells, Science 324 (2009) 71.
[3] R. Bashyam, P. Zelenay, A class of non-precious metal composite catalysts for fuel cells, Nature 44 (2006) 63.
[4] K.P. Gong, F. Du, Z.H. Xia, M. Durstock, L.M. Dai, Nitrogen-doped carbon nanotube arrays with high electrocatalytic activity for oxygen reduction, Science 323 (2009) 760.
[5] D.C. Higgins, J. Wu, W.M. Li, Z.W. Chen, Cyanamide derived thin film on carbon nanotubes as metal free oxygen reduction reaction electrocatalyst, Electrochim. Acta 59 (2012) 8.
[6] C.V. Rao, C.R. Cabrera, Y. Ishikawa, In search of the active site in nitrogen-doped carbon nanotube electrodes for the oxygen reduction reaction, J. Phys. Chem. Lett. 1 (2010) 2622.
[7] T.C. Nagaiah, S. Kundu, M. Bron, M. Muhler, W. Schuhmann, Nitrogen-doped carbon nanotubes as a cathode catalyst for the oxygen reduction reaction in alkaline medium, Electrochem. Commun. 12 (2010) 338.
[8] L. Qu, Y. Liu, J.B. Baek, L.M. Dai, Nitrogen-doped graphene as efficient metal-free electrocatalyst for oxygen reduction in fuel cells, ACS Nano 4 (3) (2010) 1321.
[9] L.P. Zhang, J.B. Niu, L.M. Dai, Z.H. Xia, Effect of microstructure of nitrogen-doped graphene on oxygen reduction activity in fuel cells, Langmuir 28 (2012) 7542.
[10] W. Xia, J. Masa, M. Bron, W. Schuhmann, M. Muhler, Highly active metal-free nitrogen-containing carbon catalysts for oxygen reduction synthesized by thermal treatment of polypyridine-carbon black mixtures, Electrochem. Commun. 13 (6) (2011) 593.
[11] S.Y. Wang, E. Iyyamperumal, A. Roy, Y.H. Xue, D.S. Yu, L.M. Dai, Vertically aligned BCN nanotubes as rfficient metal-free electrocatalysts for the oxygen reduction reaction: a synergetic effect by co-doping with boron and nitrogen, Angew. Chem. Int. Ed. 50 (2011) 11756.
[12] P.H. Matter, L. Zhang, U.S. Ozkan, The role of nanostructure in nitrogen-containing carbon catalysts for the oxygen reduction reaction, J. Catal. 239 (2006) 83.
[13] K.A. Kurak, A.B. Anderson, Nitrogen-treated graphite and oxygen electro-reduction on pyridinic edge sites, J. Phys. Chem. C 113 (2009) 6730.
[14] X.G. Li, B.N. Popova, T. Kawaharab, H. Yangai, Non-precious metal catalysts synthesized from precursors of carbon, nitrogen, and transition metal for oxygen reduction in alkaline fuel cells, J. Power Sources 196 (2011) 1717.
[15] X.J. Bo, L.P. Guo, Simple synthesis of macroporous carbon-graphene composites and their use as a support for Pt electrocatalysts, Electrochim. Acta 90 (2013) 283.
[16] J. Zeng, C. Francia, C. Gerbaldi, M.A. Dumitrescu, S. Specchia, P. Spinelli, Smart synthesis of hollow core mesoporous shell carbons (HCMSC) as effective catalyst supports for methanol oxidation and oxygen reduction reactions, J. Solid State Electrochem. 16 (2012) 3087.
[17] L. Zhang, J. Kim, E. Dy, S. Ban, K.C. Tsay, H. Kawai, Z. Shi, J. Zhang, Synthesis of novel mesoporous carbon spheres and their supported Fe-based electrocatalysts for PEM fuel cell oxygen reduction reaction, Electrochim. Acta 108 (2013) 480.
[18] L. Zhang, J. Kim, E. Dy, S. Ban, K.C. Tsay, H. Kawai, Z. Shi, J. Zhang, Effect of template size on the synthesis of mesoporous carbon spheres and their supported Fe-based ORR electrocatalysts, Electrochim. Acta 108 (2013) 814.
[19] F.B. Su, J.H. Zeng, X.Y. Bao, Y.S. Yu, J.Y. Lee, X.S. Zhao, Preparation and characterization of highly ordered graphitic mesoporous carbon as a Pt catalyst support for direct methanol fuel cells, Chem. Mater. 17 (15) (2005) 3960.
[20] H.W. Liang, W. Wei, Z.S. Wu, X.L. Feng, K. Müllen, Mesoporous metal-nitrogen-doped carbon electrocatalysts for highly efficient oxygen reduction reaction, J. Am. Chem. Soc 135 (43) (2013) 16002.
[21] Z.Y. Mo, H.L. Peng, H.G. Liang, S.J. Liao, Vesicular nitrogen doped carbon material derived from Fe_2O_3 templated polyaniline as improved non-platinum fuel cell cathode catalyst, Electrochim. Acta 99 (1) (2013) 30.
[22] H. Wang, X. Bo, Y. Zhang, L. Guo, Sulfur-doped ordered mesoporous carbon with high electrocatalytic activity for oxygen reduction, Electrochim. Acta 108 (2013) 404.
[23] R. Jasinski, A new fuel cell cathode catalyst, Nature 201 (1964) 1212.
[24] J.L. Qiao, L. Xu, L. Ding, L. Zhang, R. Baker, X.F. Dai, J.J. Zhang, Using pyridine as nitrogen-rich precursor to synthesize Co-N-S/C non-noble metal electrocatalysts for oxygen reduction reaction, Appl. Catal. B 125 (2012) 197.
[25] A. Serov, M.H. Robson, B. Halevi, K. Artyushkova, P. Atanassov, Highly active and durable templated non-PGM cathode catalysts derived from iron and aminoantipyrine, Electrochim. Acta 22 (2012) 53.
[26] C.H. Choi, S.H. Park, S.I. Woo, Heteroatom doped carbons prepared by the pyrolysis of bio-derived amino acids as highly active catalysts for oxygen electro-reduction reactions, Green Chem. 13 (2011) 406.
[27] S.A. Wohlgemuth, R.J. White, M.G. Willinger, M.M. Titirici, M. Antonietti, A one-pot hydrothermal synthesis of sulfur and nitrogen doped carbon aerogels with enhanced electrocatalytic activity in the oxygen reduction reaction, Green Chem. 14 (2012) 1515.
[28] J. Liang, Y. Jiao, M. Jaroniec, S.Z. Qiao, Sulfur and nitrogen dual-doped mesoporous graphene electrocatalyst for oxygen reduction with synergistically enhanced performance, Angew. Chem. Int. Ed. 51 (2012) 11496.
[29] Z. Liu, H.G. Nie, Z. Yang, J. Zhang, Z.P. Jin, Y.Q. Lu, Z.B. Xiao, S.M. Huang, Sulfur–nitrogen co-doped three-dimensional carbon foams with hierarchical pore structures as efficient metal-free electrocatalysts for oxygen reduction reactions, Nanoscale 5 (2013) 3283.
[30] D.W. Wang, F. Li, M. Liu, G.Q. Lu, H.M. Cheng, 3D aperiodic hierarchical porous graphitic carbon material for high-rate electrochemical capacitive energy storage, Angew. Chem. Int. Ed. 47 (2) (2007) 373.

[31] L. Wang, A. Ambrosi, M. Pumera, Metal-free catalytic oxygen reduction reaction on heteroatom-doped graphene is caused by trace metal impurities, Angew. Chem. Int. Ed. 52 (2013) 13818.
[32] F. Jaouen, J.P. Dodelet, Average turn-over frequency of O_2 electro-reduction for Fe/N/C and Co/N/C catalysts in PEFCs, Electrochimica Acta 52 (2007) 5975.
[33] I. Palchan, M. Crespin, H. Estrade-szwarckopf, B. Rousseau, Graphite fluorides of C-F bonding, Chem. Phys. Lett. 157 (4) (1989) 321.
[34] E.K. Her, T.J. Ko, B. Shin, H. Roh, W. Dai, W.K. Seong, H.Y. Kim, K.R. Lee, K.H. Oh, M.W. Moon, Superhydrophobic transparent surface of nanostructured poly (methyl methacrylate) enhanced by a hydrolysis reaction, Plasma Process. Polym. 10 (2013) 481.
[35] Z. Chen, D. Higgins, H. Tao, R.S. Hsu, Z. Chen, Highly active nitrogen-doped carbon nanotubes for oxygen reduction reaction in fuel cell applications, J. Phys. Chem. C 113 (2009) 21008.
[36] H.J. Zhang, H.C. Kong, X. Yuan, Q.Z. Jiang, J. Yang, Z.F. Ma, Influence of metal precursors on the catalytic activity and structure of non-precious metal electrocatalysts for oxygen reduction reaction, Int. J. Hydrogen Energy 37 (2012) 13219.
[37] J. Pels, F. Kapteijn, J. Moulijn, Q. Zhu, K. Thomas, Evolution of nitrogen functionalities in carbonaceous materials during pyrolysis, Carbon 33 (1995) 1641.
[38] Z. Yang, Z. Yao, G. Li, G. Fang, H. Nie, Z. Liu, X.M. Zhou, X.A. Chen, S.M. Huang, Sulfur-doped graphene as an efficient metal-free cathode catalyst for oxygen reduction, ACS nano 6 (1) (2012) 205.
[39] N. Alexeyeva, E. Shulga, V. Kisand, I. Kink, K. Tammeveski, Electroreduction of oxygen on nitrogen-doped carbon nanotube modified glassy carbon electrodes in acid and alkaline solutions, J. Electroanal. Chem. 648 (2010) 169.
[40] C.H. Choi, M.W. Chung, S.H. Park, S.I. Woo, Additional doping of phosphorus and/or sulfur into nitrogen-doped carbon for efficient oxygen reduction reaction in acidic media, Phys. Chem. Chem. Phys. 15 (2013) 1802.
[41] Q. Shi, F. Peng, S. Liao, H. Wang, H. Yu, Z. Liu, B. Zhang, D. Su, Sulfur and nitrogen co-doped carbon nanotubes for enhancing electrochemical oxygen reduction activity in acidic and alkaline media, J. Mater. Chem. A 1 (2013) 14853.
[42] C.H. Choi, M.W. Chung, Y.J. Jun, S.I. Woo, Doping of chalcogens (sulfur and/or selenium) in nitrogen-doped graphene–CNT self-assembly for enhanced oxygen reduction activity in acid media, RSC Adv. 3 (2013) 12417.
[43] S. Li, L. Zhang, J. Kima, M. Pan, Z. Shi, J.J. Zhang, Synthesis of carbon-supported binary FeCo-N non-noble metal electrocatalysts for the oxygen reduction reaction, Electrochim. Acta 55 (2010) 7346.
[44] A.B. Anderson, R.A. Sidik, Oxygen electroreduction on Fe^{II} and Fe^{III} coordinated to N_4 chelates. Reversible potentials for the intermediate steps from quantum theory, J. Phys. Chem. B 108 (2004) 5031.
[45] W. Li, A. Yu, D.C. Higgins, B.G. Llanos, Z. Chen, Biologically inspired highly durable iron phthalocyanine catalysts for oxygen reduction reaction in polymer electrolyte membrane fuel cells, J. Am. Chem. Soc. 132 (2010) 17056.
[46] S. Gupta, C. Fierro, E. Yeager, The effects of cyanide on the electrochemical properties of transition-metal macrocycles for oxygen reduction in alkaline-solutions, J. Electroanal. Chem. 306 (1991) 239.
[47] D.B. Sepa, M.V. Vojnovic, Reaction intermediates as a controlling factor in the kinetics and mechanism of oxygen reduction at platinum electrodes, Electrochim. Acta 26 (6) (1981) 781.
[48] L. Zhang, Z. Xia, Mechanisms of oxygen reduction reaction on nitrogen-doped graphene for fuel cells, J. Phys. Chem. C 115 (2011) 11170.
[49] Y. Zheng, Y. Jiao, L. Ge, M. Jaroniec, S.Z. Qiao, Two-Step Boron and Nitrogen Doping in Graphene for Enhanced Synergistic Catalysis, Angew. Chem. Int. Ed. 52 (2013) 3110.
[50] A. Bonakdarpour, M. Lefevre, R.Z. Yang, F. Jaouen, T. Dahn, J.P. Dodelet, J.R. Dahn, Impact of Loading in RRDE Experiments on Fe–N–C Catalysts: Two- or Four-Electron Oxygen Reduction? Electrochem. Solid-State Lett. 11 (6) (2008) B105.